



Effects of Temperature Distribution on Microstructure and Mechanical Properties of Hot Extruded Al–Zn–Mg–Cu Alloy Pipe with Variable Cross-Section

Lei Luo^{1,3} · Zhiyi Liu^{1,2,3} · Song Bai^{2,3} · Jing Cao^{2,3} · Fei Liu^{2,3} · Linnan Ou^{2,3} · Juangang Zhao^{2,3}

Received: 6 August 2021 / Accepted: 8 October 2021 / Published online: 11 January 2022
© The Korean Institute of Metals and Materials 2022

Abstract

The microstructures and mechanical properties of a hot extruded Al–Zn–Mg–Cu alloy pipe with variable cross-section are investigated by transmission electron microscopy, electron backscattering diffraction, hardness testing and finite element method. The results suggest that the variable temperature distribution at different positions along the extrusion direction after hot extrusion attribute to the changes in hot deformation degrees. The extruded profile at billet temperature of 410 °C and a ram speed of 1.5 mm/s shows a gradual increase in temperature from 416 to 467 °C at strains from 3.7 to 8.6 along the extrusion direction. The dynamic recovery (DRV) and partial dynamic recrystallization (DRX) are observed in the hot extruded profile, and high-angle grain boundaries fraction exponentially rises along the extrusion direction. The hardness at different positions of the hot extruded profile shows a nearly exponential decline along the extrusion direction, mainly ascribes to the decrease of the dislocation density that caused by the dynamic softening.

Keywords Al–Zn–Mg–Cu alloy · Variable cross-section pipe · Hot extrusion · FE analysis · EBSD · TEM

1 Introduction

Al–Zn–Mg–Cu alloys are widely used in aerospace, automotive and petroleum industries due to their high strength-to-weight ratios, elevated stress corrosion resistance and excellent workability [1–5].

Traditionally, steel oil drill pipes are widely applied in oil drilling industries. However, steel oil drill pipe has a high weight per unit length, and a low corrosion resistance to acid corrosion gas environments (H₂S and CO₂). Compared to conventional steel oil drill pipes, the Al–Zn–Mg–Cu alloy

oil drill pipes are advantageous in terms of high strength, low specific gravity, good fatigue resistance and resistance to acid gas corrosion like H₂S and CO₂. Hence, Al–Zn–Mg–Cu alloy oil drill pipes can reduce the energy consumption, as well as improve the drilling depth capability and electrochemical corrosion resistance in corrosive environments containing H₂S and CO₂ [1, 5]. In recent decades, with the gradual depletion of oil resources in shallow wells and the discovery of more ultra-deep oil reservoir resources, deep drilling has gradually developed into the main way of oil exploitation, and Al–Zn–Mg–Cu alloys are also considered as an ideal potential material for oil drill pipes [6]. In the past, some Al–Zn–Mg–Cu alloys with low Zn/Mg ratios have been used for oil drill pipes to improve drill depth with less energy consumption [7, 8]. The studied alloy is a newly developed aluminum alloy for oil drill pipes, due to its denser η' strengthening phase originating from high Zn/Mg ratio, which has higher strength and thermal stability than the traditional Al–Zn–Mg–Cu alloys with low Zn/Mg ratios.

During oil drilling, a long drill string composed of hundreds of oil drill pipes connected through the end is used [9]. This end of oil drill pipe possesses variable cross-section, and hot extrusion is usually utilized to process the oil drill pipe. Additionally, the microstructure of the variable

✉ Zhiyi Liu
liuzhiyi@csu.edu.cn

✉ Song Bai
baisongmse@csu.edu.cn

¹ Light Alloy Research Institute, Central South University, Changsha 410083, People's Republic of China

² School of Material Science and Engineering, Central South University, Changsha 410083, People's Republic of China

³ Key Laboratory of Nonferrous Metal Materials Science and Engineering, Ministry of Education, Central South University, Changsha 410083, People's Republic of China

section pipe plays an important role in ensuring the safety of the end of oil drill pipe, as well as the overall safety of the drill pipe. Different hot processing microstructures can present various mechanical responses [10–12]. Therefore, the microstructures and mechanical properties of hot extruded Al–Zn–Mg–Cu alloy pipes with variable cross-section are crucial information for oil drilling companies.

Hot extrusion is often employed to manufacture various kinds of Al alloy profiles [13–15]. In recent years, studies concerning the influence of hot extrusion parameters and die structures on the microstructures and mechanical properties of Al alloy profiles have attracted increasing attention [16–18]. For instance, Bharath et al. [19] investigate the microstructures and mechanical properties of extruded Al–Cu–Mg alloy solid rods under different extrusion temperatures, and reveal that the precipitate strengthening resulting from Al₂Cu (θ phase) and high-angle grain boundaries (HAGBs) fraction increases with extrusion temperature, while the dislocation density decreases. A recent work by Li et al. [20] reported that higher ram speed would lower the dynamic recrystallization (DRX) fractions of extruded 6063 alloy square hollow pipes in the welding zone as compared to the matrix zone. This may induce a larger average grain size of the welding zone as compared to the matrix zone. Sakow et al. [21] reveal that the heteromorphic extrusion die with right-angle corners can be very effective for refining Al₃Si₂Fe₂ (β phase) particles and eutectic Si particles of extruded Al–Si–Fe alloy square bar, resulting in a significant improvement in its ductility. Li et al. [22] confirm that the extruded Al–Zn–Mg–Cu alloy plate manufactured by flat die with symmetric feeder is more conducive to dynamic recovery (DRV) occurrence when compared to that fabricated by flat die without asymmetric feeder. Chen et al. [23] propose a multi-objective optimization method for feeder chamber structure, which can improve the homogeneity of flow velocity and reduce extrusion load of Al–Zn–Mg plate. Additionally, some researches on effect of heat treatment on microstructure and properties of extruded Al–Zn–Mg–Cu alloy profiles with uniform cross-section are also carried out [24, 25].

Other studies have recently focused on micro-alloying and heat treatment of Al–Zn–Mg–Cu alloys for oil drill pipes. For instance, Wang et al. [26] find that the addition of Er can improve mechanical properties as well as the intergranular corrosion resistance. As proposed by Wang et al.'s work [1], 7085 alloy can gain excellent combination of properties after a proper retrogression and re-aging (RRA) treatment. Zhao et al. [27] develop a new four-stage aging treatment for the shortcomings of traditional RRA treatment with a very short regression time so that it is not desirable to industrial production of oil drill pipes. Their data reveal that this four-stage aging treatment is beneficial to the thermal stability of Al–Zn–Mg–Cu alloy.

As mentioned above, in addition to studying the effects of hot extrusion parameters and die structures on the microstructures and mechanical properties of Al alloy uniform cross-section profiles, some reports have also investigated the influences of micro-alloying and heat treatment on the microstructures and mechanical properties of hot extruded Al–Zn–Mg–Cu alloy profiles. However, few attentions have been paid to the microstructures and their effects on mechanical properties of Al–Zn–Mg–Cu alloy variable cross-section pipe used for oil drilling. In particular, quantitative relationships among the strain, microstructures and mechanical properties of Al–Zn–Mg–Cu alloy pipe with variable cross-section used for oil drilling are lack. Such research results will be important in providing a quantitative and accurate reference for structural design, actual industrial production, microstructure control, performance evaluation and safe application of oil drill pipes.

In this work, the deformation heat ascribed to severe plastic deformation and its effects on temperature distribution, as well as the influence of temperature distribution on microstructure, are discussed. The quantitative relationships between strain and hardness, as well as strain and HAGBs fraction, are investigated using several experimental techniques coupled with the finite element (FE) method.

2 FE Analysis

In present work, the hot extrusion process for Al–Zn–Mg–Cu alloy pipe with variable cross-section is simulated by DEFORM-3D commercial software based on FE method. The schematic diagram of hot extrusion process and corresponding FE model is presented in Fig. 1a. The extrusion tools, such as the container, ram and die were all defined to be rigid, and the billet was regarded as plastic. The dimensions of extruded profile can be seen in Fig. 1b. The physical properties of studied Al–Zn–Mg–Cu alloy and H13 tool steel were summarized in Table 1. Automatic meshing was used in FE simulation, and FE simulation parameters are given in Table 2.

In our previous work, a constitutive model based on strain compensation of studied Al–Zn–Mg–Cu alloy was established from hot compression test as expressed in Eq. (1) [31]. This constitutive model was introduced into DEFORM-3D as basic data, and then the FE analysis hot extrusion process on Al–Zn–Mg–Cu alloy pipe with variable cross-section is carried out.

$$\begin{cases} Z = \dot{\epsilon} \exp\left(\frac{Q(\epsilon)}{8.314T}\right) = A(\epsilon)[\sinh(\alpha(\epsilon)\sigma)]^{n(\epsilon)} \\ \sigma = \frac{1}{\alpha(\epsilon)} \ln\left\{\left(\frac{Z(\epsilon)}{A(\epsilon)}\right)^{\frac{1}{n(\epsilon)}} + \left[\left(\frac{Z}{A(\epsilon)}\right)^{\frac{2}{n(\epsilon)}} + 1\right]^{\frac{1}{2}}\right\} \end{cases} \quad (1)$$

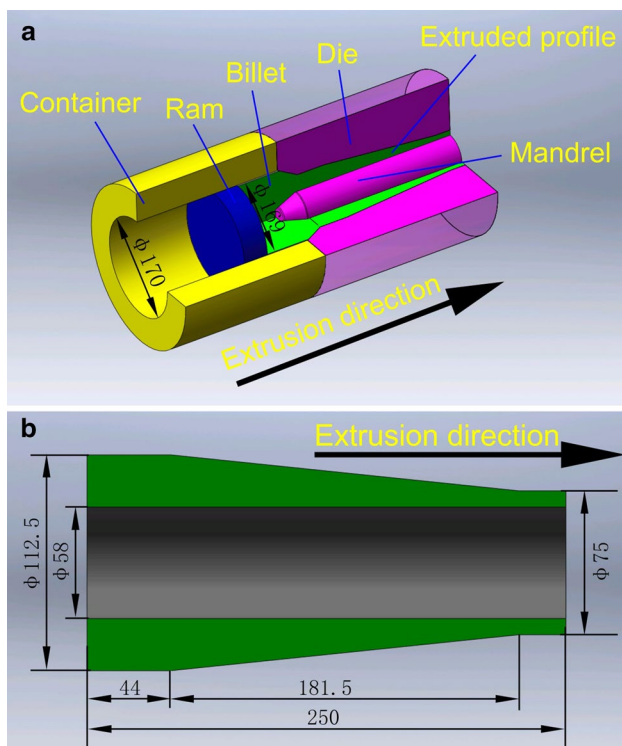


Fig. 1 a Schematic diagram of hot extrusion process and corresponding FE model. b The dimensions of extruded profile. (Unit: mm)

Table 1 Physical properties of Al–Zn–Mg–Cu alloy and H13 tool steel [22, 28, 29]

Properties	Al–Zn–Mg–Cu alloy	H13 tool steel
Young's modulus (GPa)	70	210
Poisson's ratio	0.3	0.3
Heat capacity (N/(mm ² ·°C))	2.4	5.6
Thermal conductivity (N/(s·°C))	180	28.4

Table 2 Numerical simulation parameters used in this work

Parameters	Values
Total number of elements	156,000
Billet temperature (°C)	410
Tooling temperature (°C)	390
Ram speed (mm/s)	1.5
Friction factor	0.3
Heat transfer coefficient between billet and tooling (N/(s mm·°C))	11 [29, 30]
Heat transfer coefficient between billet/ tooling and air (N/(s mm·°C))	0.02 [29, 30]

3 Experimental Procedures

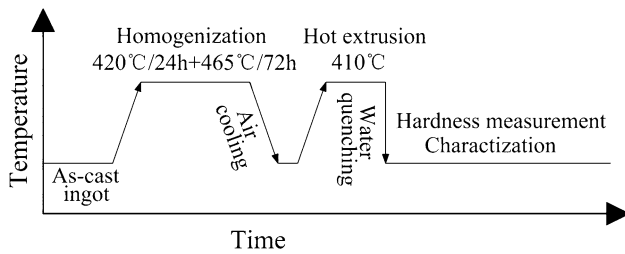
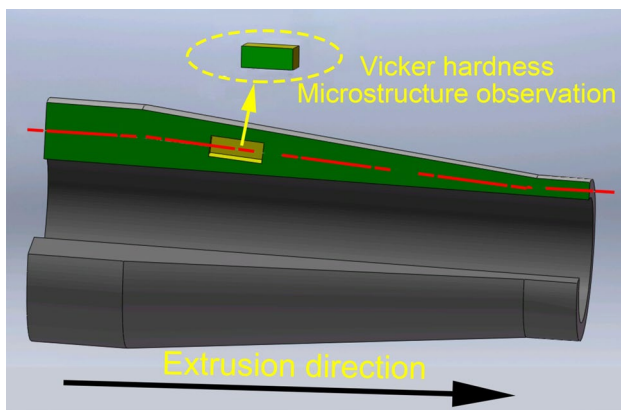
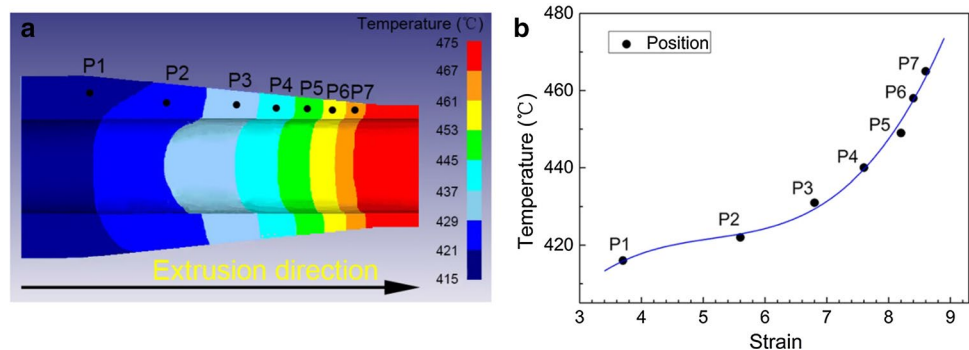
The chemical composition of the studied Al–Zn–Mg–Cu alloy was summarized in Table 3.

The studied Al–Zn–Mg–Cu alloy was subjected to several experiments, including homogenization, hot extrusion, Vicker hardness testing and microstructure characterization. Figure 2 schematically shows the diagram for whole experiment period. The as-cast ingot was first subjected to a two-step homogenization (420 °C/24 h + 465 °C/72 h) followed by slowly cooled down to room temperature under air. Next, the homogenized ingot with a diameter of 200 mm was machined to cylindrical billet with the dimension of $\Phi 169 \times 150$ mm used for hot extrusion. The schematic diagram of hot extrusion process was given in Fig. 1a. The extrusion setup was assembled by the ram, container and die. These components were machined by H13 tool steel. The inner diameter of container was $\Phi 170$ mm, and the extrusion ratio changed continuously from 3.1 to 12.7. All hot extrusion experimental parameters were fully consistent with FE simulation parameters in Table 2. After the extrusion, the extruded Al–Zn–Mg–Cu alloy pipe with variable cross-section was immediately water quenched. For microstructure observation and Vickers hardness testing, samples were cut from the central location of the wall thickness of pipe with variable cross-section along the extrusion direction (Fig. 3). Detailed sampling positions based on FE analysis data were shown in Fig. 4a, and named as P1, P2, P3, P4, P5, P6 and P7, respectively. The main aim of that was to investigate the effects of different temperature distribution of extruded profile on the microstructures and mechanical properties.

The Vickers hardness measurements were carried out using an 8 kgf loading on an HMV-2 sclerometer for 15 s. The microstructure observation of the samples was performed by transmission electron microscopy (TEM, FEI Tecnai G² 20) operated at 200 kV, as well electron backscattering diffraction (EBSD) installed on a ZEISS EVOMA scanning electron microscopy (SEM). The EBSD data was analyzed by TSL OIM Analysis 5 software. The TEM samples were first ground to approximately 100 μ m followed by punching into discs with 3 mm in diameter, and then electro-polishing with twin-jet equipment at voltage of 15 V in a 20% HNO₃ and 80% CH₃OH solution at about – 25 °C for about 150 s. The preparation method of EBSD samples was the same as that of TEM samples, except that the electro-polishing time used (about 105 s) was shorter than that of TEM samples.

Table 3 Chemical composition of the studied Al–Zn–Mg–Cu alloy (in wt%)

Composition	Zn	Mg	Cu	Mn	Cr	Ti	Si	Fe	Al
Content	6.96	2.39	1.76	0.41	0.16	0.09	0.01	0.06	Bal

**Fig. 2** Schematic diagram summarizing the whole experiment period of studied Al–Zn–Mg–Cu alloy**Fig. 3** Microstructure observation and Vicker hardness testing location of extruded profile**Fig. 4** **a** Temperature distribution with sampling position obtained by numerical simulation at the end of extrusion process. **b** Temperature variation of different positions for extruded profile derived by curve fitting

4 Results

4.1 Temperature Profiles

The temperature distribution of the extruded Al–Zn–Mg–Cu alloy pipe with variable cross-section at

the end of extrusion process is displayed in Fig. 4a. It can be found that the temperature distribution along the extrusion direction is inhomogeneous, and the temperature gradient is generated. To further accurately expose the simulation results, the temperature and strain of seven positions (P1–P7 in Fig. 4a) are obtained through the point tracking function of DEFORM-3D software. Then, the relationships between temperature and strain of different positions in extruded profile are gained by curve fitting, as shown in Fig. 4b. It can be seen that the temperature increases with the strain, and the maximum and minimum values identified as 467 °C and 416 °C, respectively. The peak temperature rise (ΔT) inside the whole extruded profile is 51 °C, which is larger than the value 8 °C of Al–Cu–Li alloy with 450 °C billet temperature and 0.25 mm/s ram speed found by Xu et al. [32], while lower than the value 120 °C of CP-Ti with 450 °C billet temperature reported by Jiang et al. [33]. Such differences in ΔT may be attributed to the variation of extrusion ways, ram speeds, billet temperatures, extruded profile geometry and material properties.

4.2 Mechanical Properties

The variations in hardness as a function of strain at different positions of the extruded profile are shown in Fig. 5. It can be clearly found that as strain increases, the hardness decreases. Besides, the hardness declines slightly from

121.8 to 114.6 as the strain rises from 3.7 (P1) to 6.8 (P3), then the hardness diminishes rapidly from 114.6 to 94.6 as strain increases from 6.8 (P3) to 8.6 (P7). Simultaneously, the curve fitting also shows a nearly exponential relationship between hardness and strain. The curve fitting results can be expressed as Eq. (2).

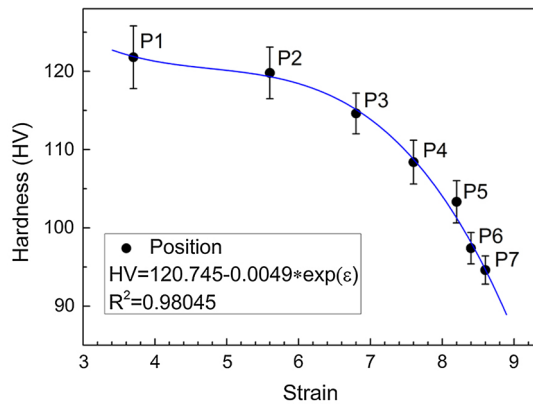


Fig. 5 Hardness-strain curve illustrating the variation of the mechanical properties at different positions of extruded profile

$$HV = 120.745 - 0.0049 * \exp(\varepsilon) \quad (2)$$

where HV is Vicker hardness and ε represents strain.

4.3 Microstructure Characterization

Bright field TEM images in Fig. 6 show microstructures at various positions of extruded Al–Zn–Mg–Cu alloy pipe with variable cross-section. As shown in Fig. 6a–c, as the strain increases from 3.7 (P1) to 6.8 (P3), the dislocation density decreases slightly, and numerous high-density dislocation tangles are within the deformed grains. Compared to Fig. 6a–c, the lower dislocation densities are observed in Fig. 6d–g. Also, the dislocation density decreases rapidly with strain increases from 6.8 (P3) to 8.6 (P7). Meanwhile, the cell structures, subgrains, HAGBs and DRX grains are gradually generated as the strain increases from 3.7 (P1) to 8.6 (P7).

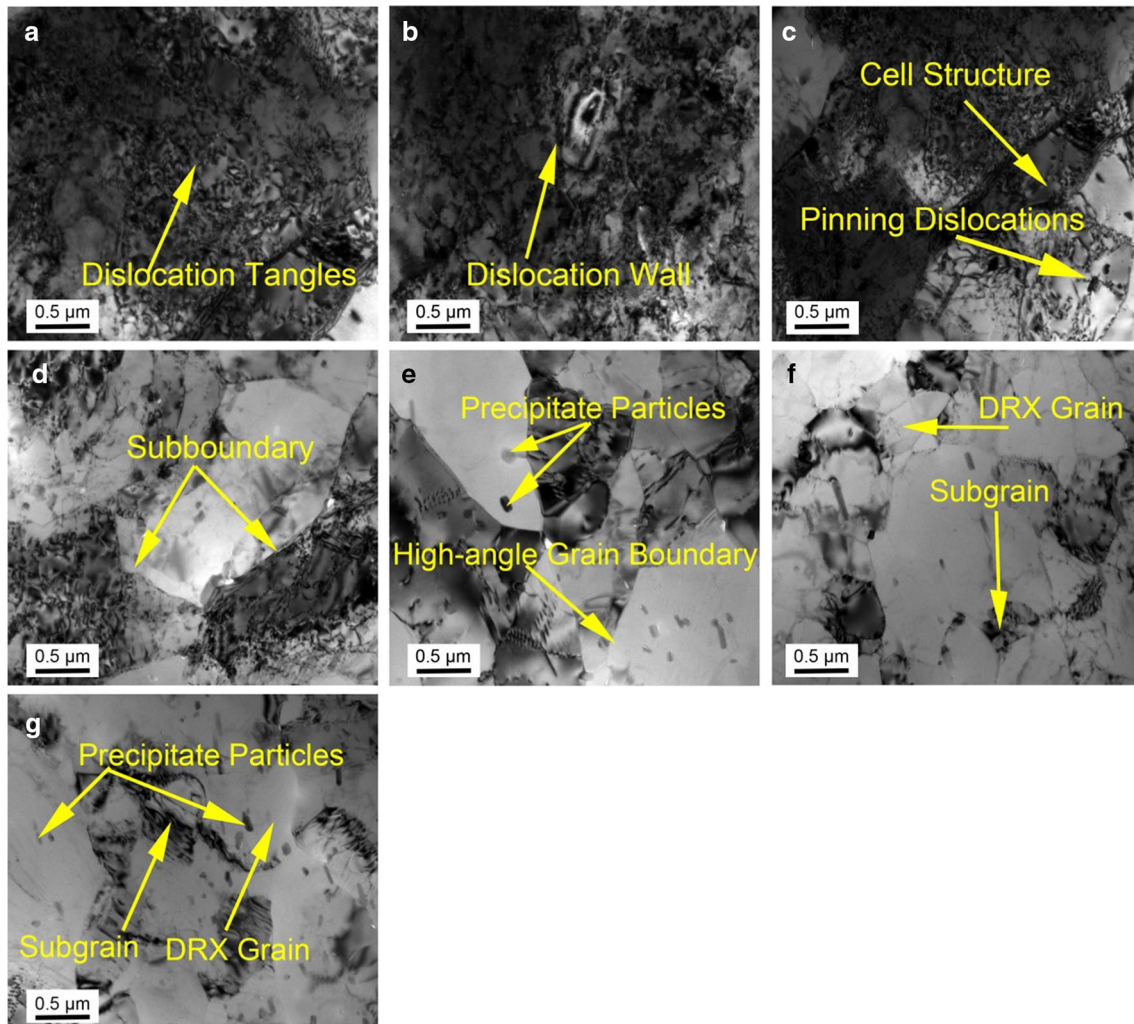


Fig. 6 TEM images at various positions of the extruded profile: **a** P1, **b** P2, **c** P3, **d** P4, **e** P5, **f** P6, and **g** P7

Additionally, a variety of second-phase particles are distributed in the interior of microstructures, as seen in Fig. 6. These precipitates are identified in previous works as $MgZn_2$ [31, 34–36]. The average sizes of precipitates are 61.2 ± 0.2 nm, 61.1 ± 0.3 nm, 61.7 ± 0.3 nm, 62.5 ± 0.7 nm, 63.1 ± 0.9 nm, 63.9 ± 0.4 nm and 64.3 ± 0.5 nm for the positions of P1, P2, P3, P4, P5, P6 and P7, respectively. As mentioned above, the average size of precipitates increases slightly as the strain increases from 3.7 (P1) to 8.6 (P7).

EBSD maps of various positions of extruded Al–Zn–Mg–Cu alloy pipe with variable cross-section are illustrated in Fig. 7. Note that the green lines represent low-angle grain boundaries (LAGBs, $2-5^\circ$), the red lines indicate medium angle boundaries (MAGBs, $5-15^\circ$), and the black lines symbolize HAGBs ($> 15^\circ$). The microstructures at different positions of extruded profile are mainly composed of elongated strip-shaped grains resulted from compressive pressure and fine equiaxed grains, as shown in Fig. 7. As the strain rises from 3.7 (P1) to 8.6 (P7), the ratio of

width to length of the elongated strip-shaped grains gradually decreases, while the number of fine equiaxed grains gradually increases. The average grain sizes are counted as 13.0 μ m, 12.1 μ m, 11.8 μ m, 10.1 μ m, 9.1 μ m, 8.5 μ m and 8.2 μ m for the positions of P1, P2, P3, P4, P5, P6 and P7, respectively. The average grain size gradually decreases as strain rises from 3.7 (P1) to 8.6 (P7) along the extrusion direction. The misorientation angle distribution of the grain boundaries at various positions is given in Fig. 8. The fractions of HAGBs at positions P1, P2, P3, P4, P5, P6 and P7 are calculated as 21.1%, 23.5%, 28.6%, 32.2%, 37.5%, 41.7% and 42.9%, respectively. This meant that DRV and partial DRX take place during the extrusion profile. In general, the fractions of HAGBs gradually enhances with strain.

The variation of HAGBs fraction as a function of strain at different positions of extruded profile can be obtained by curve fitting. As shown in Fig. 9, the HAGBs fraction increases slightly from 21.1% to 28.6% as strain rises from 3.7 (P1) to 6.8 (P3). By comparison, HAGBs fraction

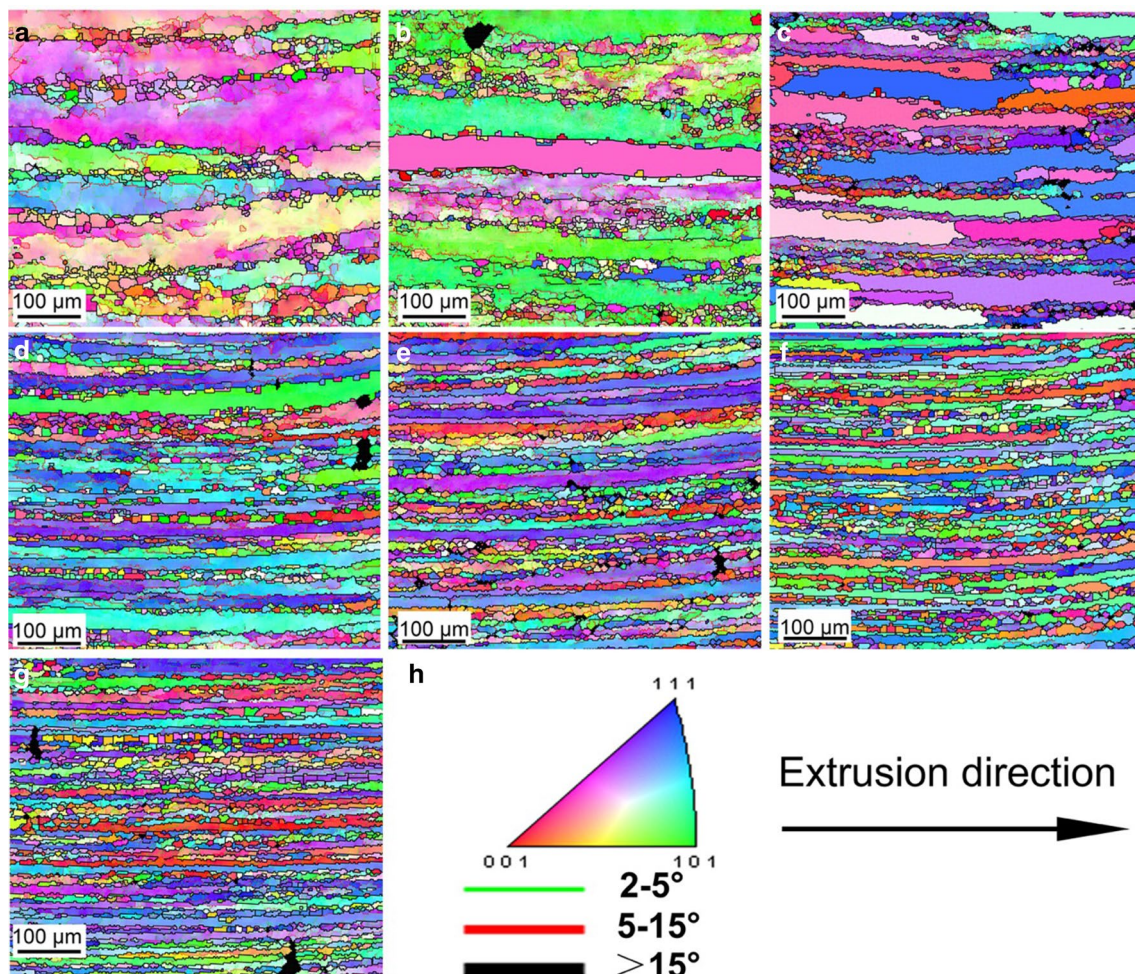


Fig. 7 EBSD micrographs of: **a** P1, **b** P2, **c** P3, **d** P4, **e** P5, **f** P6, and **g** P7. **h** Inverse pole figure (IPF) and color lines utilized to recognize the boundaries with different misorientation angles in (a–g)

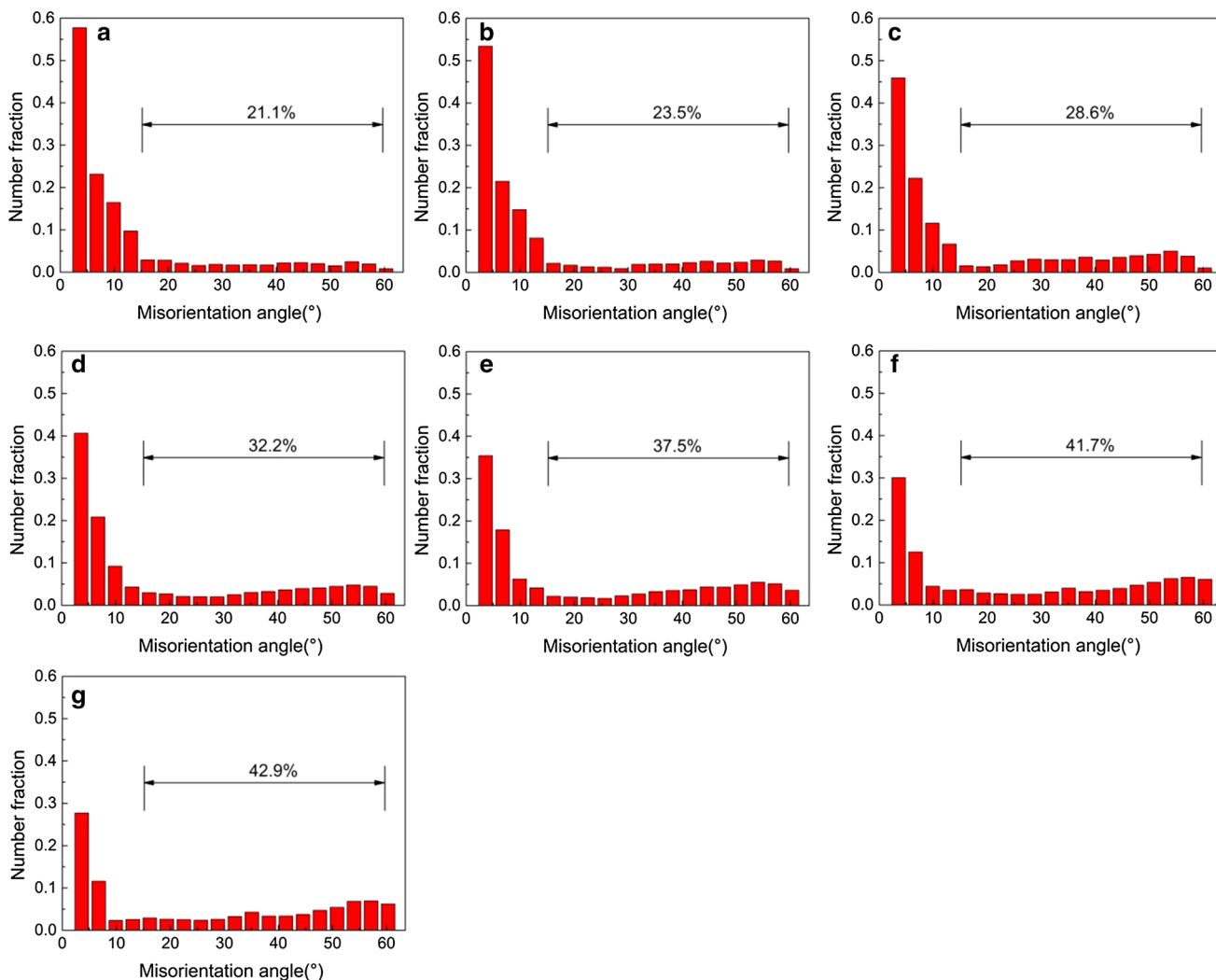


Fig. 8 Misorientation angle distributions of various positions of the extruded profile: **a** P1, **b** P2, **c** P3, **d** P4, **e** P5, **f** P6, and **g** P7

increases remarkably from 28.6% to 42.9% as the strain increases from 6.8 (P3) to 8.6 (P7), as shown in Fig. 9. The maximum HAGBs fraction is 42.9%. Moreover, an approximately exponential relationship between HAGBs fraction and strain is obtained through curve fitting, and the fitting results can be represented as Eq. (3).

$$F = 20.0425 + 0.0041 * \exp(\epsilon) \tag{3}$$

where F represents fraction of HAGBs and ϵ is strain.

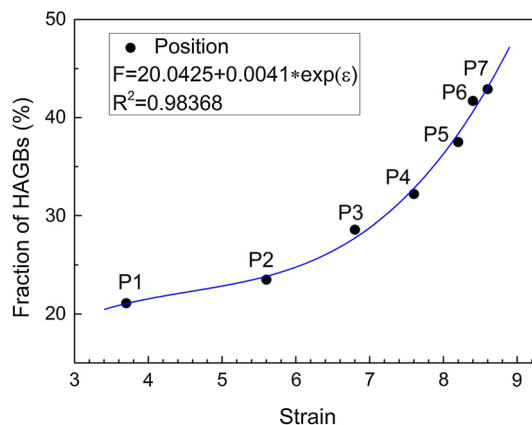


Fig. 9 HAGBs fraction-strain curve showing the variation of misorientation angle at different positions of the extruded profile

5 Discussion

5.1 Effect of Deformation Degree on Temperature Distribution

The different temperature distribution along the extrusion direction of extruded Al–Zn–Mg–Cu alloy pipe with variable cross-section resulting from the different strains at different positions of the extruded profile. The degree of deformation increases gradually along the extrusion direction, thereby leading to a gradual increase in strain along the extrusion direction. The deformation heat varies proportional to the strain, and deformation heat is converted to the increased temperature of the extruded profile [37–39]. Thus, the temperature gradually rises along the extrusion direction of the extruded profile as seen in Fig. 4a. Besides, the temperature rise converted from the deformation heat of the small cross-sectional domain material occurred earlier than the large cross-sectional domain material deformed later during extrusion. As extruding continues, the material from the small cross-sectional domain becomes deformed at higher temperatures during subsequent extrusion when compared to the material from the large cross-sectional domain, gaining a higher temperature raise. During the extrusion process, the strain increases with the decrease in the cross-section area of the extruded material at constant ram speed of 1.5 mm/s. This results in a gradual increase in the strain rate. The heat loss transfer from the material to the die is inversely proportional to the strain rate. The material can be regarded as adiabatic at extremely high strain rate [40–42]. Hence, the low strain rate regions (P1, P2 and P3 positions) have higher heat loss as compared to the high strain rate regions (P4, P5, P6 and P7 positions). Simultaneously, the heat loss increases with the increasing contact area between the material and die. From Fig. 4a, it is clearly observed that the contact area between the material and die in the isothermal region at P1, P2 and P3 positions is larger than that at P4, P5, P6 and P7 positions. As a result, the region at the P1, P2 and P3 positions possesses more heat loss than at P4, P5, P6 and P7 positions. In sum, it is not surprising to find from Fig. 4b that a slight temperature increases from P1 to P3 followed by a remarkable enhancement from P3 to P7.

5.2 Effect of Temperature on Microstructure Evolution

The microstructure of extruded Al–Zn–Mg–Cu alloy pipe with variable cross-section is closely related to its temperature distribution. The movement of dislocations in

metal materials can be regarded as a thermally activated process [43, 44]. At lower temperatures, the thermal activation effect is small, and the effect of hindering dislocation movement is great, so that the efficiency of dislocation climb and cross-slip is low, resulting in high-density dislocation tangles, cell structures and dislocation walls in the deformed grain interior. Nevertheless, higher temperatures will intensify the thermal activation effect and weaken the resistance of dislocation movement. This will accelerate the dislocation annihilation and rearrangement caused by climbing and cross-slipping. As a result, the number of subgrain with LAGBs formed by segmenting elongated grains through dislocation walls increases. When the energy exceeds the critical value of DRX, the migration of subgrain boundaries is promoted, and new fine equiaxed DRX grains are facilitated. Hence, the conversion from DRV to DRX become intensified, and LAGBs are gradually transformed into HAGBs. Naturally, the dislocation density gradually decreases and the number of fine equiaxed DRX grains gradually increases along the extrusion direction (P1–P7). This, in turn, increases the fraction of HAGBs. Simultaneously, since the billet temperature is only 410 °C and the temperature at the highest temperature position (P7) of the extruded profile is 467 °C, the energy for dislocation movement is only enough for DRV and partial DRX, but insufficient for complete DRX. As a result, only a few LAGBs are transformed into HAGBs. Therefore, as shown in EBSD results of present work, the HAGBs fractions at different positions are relatively small when compared to the LAGBs fractions. The majority of the grain boundaries belong to LAGBs, indicating that microstructural evolution is mainly DRV and partial DRX during hot extrusion. In sum, higher temperature plays a positive effect on the transformation from LAGBs into HAGBs.

The maximum value of HAGBs fraction is recorded as 42.9% in this work, lower than the minimum value 64.77% of HAGBs fraction of Al–Zn–Mg alloys in the welding zone of extruded profile reported by Chen et al. [3]. This is attributed to the material in the welding zone, which is subjected to higher hot extrusion deformation than the studied alloy. Firstly, the higher degree of deformation, the larger dislocation density stemmed from the dislocation piles up and multiplies rapidly, it can accumulate more energy for DRX and hence DRX is improved. Secondly, a larger number of dislocations are generated with an enhanced higher degree of deformation. This provides much more subgrains by dislocation movement, forming more DRX grains from subgrains [45–47]. Finally, a larger amount of deformation heat is generated from greater the deformation degrees, providing more energy for DRX and further improving the occurrence of DRX. As a result, the reported material in the welding zone by Chen et al. has a larger HAGBs fraction

when compared to the present work. Meanwhile, Fang et al. record [48] only about 20% HAGBs fraction of T6 tempered Al–Zn–Mg–Cu–Zr alloy extruded profiles, while the maximum of 42.9% in present work is much higher than 20%. The reason for this difference is related to the addition of 0.3Zr (wt%) in Fang et al.'s work. As a result, fine and coherent Al₃Zr particles are formed during homogenization. Al₃Zr particles show a strong pinning effect on dislocations and subgrain boundaries, hindering the movement of dislocations and subgrain boundaries, as well as weakening DRX. Therefore, the HAGBs fraction maximum of 42.9% in present work is higher than the 20% reported by Fang et al. [48].

5.3 Effect of Microstructure on Mechanical Properties

The different mechanical properties at distinct positions of extruded Al–Zn–Mg–Cu alloy pipe with variable cross-section are attributed to microstructural variations after extrusion. In this work, precipitation strengthening effects at different positions of extruded profiles have no significantly difference as the precipitates size is almost identical. Therefore, the mechanical properties at different positions of the extruded profile are determined by the combined effects of grain boundary and dislocation strengthening.

According to the Hall–Petch equation, the grain boundary strengthening $\Delta\sigma_{gb}$ can be expressed by Eq. (4) [49].

$$\Delta\sigma_{gb} = k_y 1/\sqrt{D} \quad (4)$$

where k_y is Hall–Petch coefficient, for Al–Zn–Mg–Cu alloys k_y is about 0.09 MPa \sqrt{m} [50, 51], D the average grain size, $\Delta\sigma_{gb}$ is proportional to $1/\sqrt{D}$. As clearly seen in the EBSD results (Figs. 7 and 8), the degree of DRX gradually increases along the extrusion direction, while the average grain size gradually decreases from 13.0 μm to 8.2 μm , and hence resulting in the strength increased. The values for average grain size at various positions are applied in Eq. (4), the grain boundary strengthening $\Delta\sigma_{gb}$ are calculated to be 25.0 MPa, 25.9 MPa, 26.2 MPa, 28.3 MPa, 29.8 MPa, 30.9 MPa and 31.6 MPa, respectively. In the above result, the grain boundary strengthening $\Delta\sigma_{gb}$ increases 6.6 MPa as strain rises from 3.7 (P1) to 8.6 (P7).

Moreover, the Taylor-model can be used to express the relationship between dislocation strengthening $\Delta\sigma_d$ and dislocation density ρ of metal materials [52–54]:

$$\Delta\sigma_d = M\alpha Gb\sqrt{\rho} \quad (5)$$

where M is Taylor factor, α represents a constant related to dislocation states, G refers to the shear modulus, and b is the Burgers vector.

The dislocation density of aluminum alloy after severe deformation is 10^{14} – 10^{15} mm^{-2} [53, 55]. Equation (5) indicates weaken strength with decreasing dislocation density. Meanwhile, comparing EqS. (4) and (5), it is easy to find that the k_y using in Eq. (4) is only about 0.09 MPa \sqrt{m} , while the ρ in Eq. (5) is 10^{14} – 10^{15} mm^{-2} . Meanwhile, in view of the above result, the grain boundary strengthening $\Delta\sigma_{gb}$ increases only 6.6 MPa as strain rises from 3.7 (P1) to 8.6 (P7). Consequently, grain boundary strengthening may be very small when compared to dislocation strengthening. Hence, dislocation strengthening plays a major role in the mechanical properties of extruded profile. The increase in strength caused by grain boundary strengthening is far from compensating for the decrease in strength caused by the decrease in dislocation density. As a result, the strength changing trend at different positions depends on the dislocation strengthening. As shown in Fig. 6, the dislocation densities at P1, P2 and P3 positions are much higher than those at P4, P5, P6 and P7 positions, leading to a decrease of the strength along the extrusion direction (P1–P7). In addition, the decrease of dislocation density is a result of dynamic softening and HAGBs fraction can reflect the degree of dynamic softening. EBSD results also show an increasing trend of HAGBs fraction along the extrusion direction (P1–P7) with a nearly exponential curve. Hence, a decrease in dislocation density may also follow an exponential trend. Thus, the combined effect of the above two factors (dislocation strengthening and dynamic softening) leads to the declined hardness along the extrusion direction (P1–P7) with approximate exponential variation.

In summary, it is necessary to keep in mind that the microstructures and mechanical properties in the extruded profile may be inhomogeneous when using some ways to investigate extruded Al–Zn–Mg–Cu alloy variable cross-section pipe.

6 Conclusions

In this work, an Al–Zn–Mg–Cu alloy pipe with variable cross-section is processed by hot extrusion. The microstructures and mechanical properties of the extruded profile at different positions are investigated. The following conclusions can be drawn:

- (1) The materials at different positions of the pipe with variable cross-section are subjected to various degrees of deformation, resulting in different deformation heats by extrusion. At the billet temperature of 410 °C with a ram speed of 1.5 mm/s, the strain along the extrusion direction increases from 3.7 (P1) to 8.6 (P7), the temperature gradually enhances from 416 °C (P1) to 467 °C (P7).

- (2) The DRV and partial DRX have occurred in the extruded pipe with variable cross-section. The HAGBs fraction rises along the extrusion direction following an approximate exponential variation. The exponential relationship between HAGBs fraction and strain can be expressed by:

$$F = 20.0425 + 0.0041 * \exp(\epsilon)$$

- (3) As the strain along the extrusion direction increases from 3.7 (P1) to 8.6 (P7), the hardness of the extruded pipe with variable cross-section firstly decreases slightly and then decreases rapidly, which is similar to the change trend of the exponential curve. The exponential relationship between hardness and strain can be expressed by:

$$HV = 120.745 - 0.0049 * \exp(\epsilon)$$

- (4) The hardness at different positions of extruded pipe with variable cross-section along extrusion direction is mainly determined by the change in dislocation density caused by dynamic softening.

Acknowledgements The authors are grateful for the financial support from the National Key Research and Development Program of China (2016YFB0300900), the National Key Fundamental Research Project of China (2012CB619506-3), National Natural Science Foundation of China (51171209).

Author contribution Lei Luo: Methodology, Investigation, Writing-original draft. Zhiyi Liu: Supervision, Writing-review & editing. Song Bai: Supervision, Writing-review & editing. Jing Cao: Writing-review & editing. Fei Liu: Writing-review & editing. Linnan Ou: Writing-review & editing. Juangang Zhao: Writing-review & editing

Declaration

Conflict of interest The authors declare that they have no known competing financial interests or personal relationships that could have appeared to influence the work reported in this paper.

References

1. Y.C. Wang, L.F. Cao, X.D. Wu, X. Tong, B. Liao, G.J. Huang, Z.G. Wang, *J. Alloy. Compd.* **814**, 152264 (2020)
2. M.A. Khan, Y.W. Wang, M.J. Anjum, G. Yasin, A. Malik, F. Nazeer, S. Khan, T. Ahmad, H. Zhang, *Vacuum* **174**, 109185 (2020)
3. L. Chen, G.J. Chen, J.W. Tang, G.Q. Zhao, C.S. Zhang, *Mater. Charact.* **158**, 109953 (2019)
4. E.M. Mazzer, C.R.M. Afonso, C. Bolfarini, C.S. Kiminami, *Intermetallics* **43**, 182 (2013)
5. C. Feng, W.B. Shou, H.Q. Liu, D.Q. Yi, Y.R. Feng, *T. Nonferr. Metal. Soc.* **25**, 3515 (2015)
6. Y.C. Wang, L.F. Cao, X.D. Wu, Y. Zou, G.J. Huang, *Materials Reports* **33**, 1190 (2019)
7. J. Liang, J.H. Sun, X.M. Li, Y.Q. Zhang, L. Peng, *Procedia Eng.* **73**, 84 (2014)
8. J.C. Liu, M.J. Qin, Q.L. Zhao, L. Chen, P.F. Liu, J.G. Gao, *Thin-Walled Struct.* **111**, 155 (2017)
9. C. Santus, *Int. J. Fatigue* **30**, 677 (2008)
10. J.H. Zhao, Y.L. Deng, J.G. Tang, J. Zhang, *J. Alloy. Compd.* **809**, 151788 (2019)
11. Y. Guo, J.H. Zhang, H.W. Zhao, *J. Mater. Sci.* **56**, 13429 (2021)
12. A. Ghosh, M. Ghosh, K. Gudimetla, R. Kalsar, L.A.I. Kestens, C.S. Kondaveeti, B.S. Pugazhendhi, B. Ravisankar, *Arch. Civ. Mech. Eng.* **20**, 7 (2020)
13. J.Q. Yu, G.Q. Zhao, C.S. Zhang, L. Chen, *Mater. Sci. Eng. A* **682**, 679 (2017)
14. H.A. Godinho, A.L.R. Beletati, E.J. Giordano, C. Bolfarini, *J. Alloy. Compd.* **586**, S139 (2014)
15. A.R. Eivani, H.R. Jafarian, J. Zhou, *J. Manuf. Process.* **57**, 881 (2020)
16. M.A. Khan, Y.W. Wang, G. Yasin, F. Nazeer, A. Malik, W.Q. Khan, T. Ahmad, H. Zhang, M.A. Afifi, *Mater. Charact.* **167**, 110472 (2020)
17. S. Kaneko, K. Murakami, T. Sakai, *Mater. Sci. Eng. A* **500**, 8 (2009)
18. X. Xu, G.Q. Zhao, Y.X. Wang, X.X. Chen, C.S. Zhang, *Vacuum* **167**, 28 (2019)
19. K. Bharath, A. Mandal, A. Karmakar, A.K. Khanra, M.J. Davidson, *Mater. Charact.* **170**, 110715 (2020)
20. S.K. Li, L.X. Li, H. He, Z.W. Liu, L. Zhang, *T. Nonferr. Metal. Soc.* **29**, 1803 (2019)
21. S. Sakow, T. Tokunaga, M. Ohno, K. Matsuura, *J. Mater. Process. Tech.* **277**, 116447 (2020)
22. Y.Q. Li, L. Chen, J.W. Tang, G.Q. Zhao, C.S. Zhang, *J. Alloy. Compd.* **749**, 293 (2018)
23. L. Chen, Y.Q. Li, G.Q. Zhao, C.S. Zhang, F.Z. Gao, *J. Mater. Res. Technol.* **9**, 507 (2020)
24. G.J. Chen, L. Chen, G.Q. Zhao, C.S. Zhang, *J. Alloy. Compd.* **729**, 210 (2017)
25. Z.G. Li, L. Chen, J.W. Tang, W.C. Sun, G.Q. Zhao, C.S. Zhang, *J. Alloy. Compd.* **863**, 158725 (2021)
26. Y.C. Wang, X.D. Wu, L.F. Cao, X. Tong, M.J. Couper, Q. Liu, *Mater. Sci. Eng. A* **792**, 139807 (2020)
27. J.G. Zhao, Z.Y. Liu, S. Bai, T.T. Huang, J. Wang, H.Y. Xie, D.P. Zeng, L. Luo, *Mater. Sci. Eng. A* **803**, 140490 (2021)
28. G.J. Chen, L. Chen, G.Q. Zhao, C.S. Zhang, W.C. Cui, *J. Alloy. Compd.* **710**, 80 (2017)
29. A.R. Eivani, J. Zhou, *J. Alloy. Compd.* **725**, 41 (2017)
30. F. Li, H.B. Wu, M.H. Qin, *Mod. Phys. Lett. B* **30**, 1650053 (2016)
31. L. Luo, Z.Y. Liu, S. Bai, J.G. Zhao, D.P. Zeng, J. Wang, J. Cao, Y.C. Hu, *Materials* **13**, 1743 (2020)
32. X. Xu, X.W. Ma, G.Q. Zhao, X.X. Chen, Y.X. Wang, *J. Alloy. Compd.* **867**, 159043 (2021)
33. H. Jiang, Z.G. Fan, C.Y. Xie, *Mater. Sci. Eng. A* **513-514**, 109 (2009)
34. Z.C. Sun, H.L. Wu, J. Cao, Z.K. Yin, *Int. J. Plasticity* **106**, 73 (2018)
35. Y.D. Zhang, S.B. Jin, P.W. Trimby, X.Z. Liao, M.Y. Murashkin, R.Z. Valiev, J.Z. Liu, J.M. Cairney, S.P. Ringer, G. Sha, *Acta Mater.* **162**, 19 (2019)
36. J.F. Jiang, Y. Wang, Y.Z. Liu, G.F. Xiao, H. Li, *T. Nonferr. Metal. Soc.* **31**, 609 (2021)
37. D.L. Baragar, *J. Mech. Work. Technol.* **14**, 295 (1987)
38. P.L. Charpentier, B.C. Stone, S.C. Ernst, J.F. Thomas, *Metall. Trans. A* **17**, 2227 (1986)
39. R.L. Goetz, S.L. Semiatin, *J. Mater. Eng. Perform.* **10**, 710 (2001)
40. Q.X. Pei, B.H. Hu, C. Lu, Y.Y. Wang, *Scripta Mater.* **49**, 303 (2003)

41. L. Li, J. Zhou, J. Duszczyn, J. Mater. Process. Tech. **172**, 372 (2006)
42. D.M. Neto, V.M. Simões, M.C. Oliveira, J.L. Alves, H. Laurent, A. Oudriss, L.F. Menezes, Mech. Mater. **146**, 103398 (2020)
43. J.C. Long, Q.X. Xia, G.F. Xiao, Y. Qin, S. Yuan, Int. J. Mech. Sci. **191**, 106069 (2021)
44. J.J. Zhang, Y.P. Yi, S.Q. Huang, X.C. Mao, H.L. He, J.G. Tang, W.F. Guo, F. Dong, Mater. Sci. Eng. A **804**, 140650 (2021)
45. O. Sitdikov, R. Garipova, E. Avtokratova, O. Mukhametdinova, M. Markushevet, J. Alloy. Compd. **746**, 520 (2018)
46. Y.J. Lang, Y.H. Cai, H. Cui, J.S. Zhang, Mater. Design **32**, 4241 (2011)
47. J.H. Zhao, Y.L. Deng, J.G. Tang, J. Zhang, Mater. Sci. Eng. A **798**, 139927 (2020)
48. H.C. Fang, H. Chao, K.H. Chen, Mater. Sci. Eng. A **610**, 10 (2014)
49. Z.G. Chen, Z.G. Yuan, J.K. Ren, J. Alloy. Compd. **828**, 154446 (2020)
50. M.J. Starink, S.C. Wang, Acta Mater. **51**, 5131 (2003)
51. L.J. Zheng, C.Q. Chen, T.T. Zhou, P.Y. Liu, M.G. Zeng, Mater. Charact. **49**, 455 (2002)
52. H. Mecking, U.F. Kocks, Acta Mater. **29**, 1865 (1981)
53. X. Chen, D.B. Xia, J.L. Zhang, G.S. Huang, K. Liu, A.T. Tang, B. Jiang, F.S. Pan, J. Alloy. Compd. **846**, 156306 (2020)
54. R.Q. Lu, S.W. Zheng, J. Teng, J.M. Hu, D.F. Fu, J.C. Chen, G.D. Zhao, F.L. Jiang, H. Zhang, J. Mater. Sci. Technol. **80**, 150 (2021)
55. M. Reihanian, R. Ebrahimi, N. Tsuji, M.M. Moshksar, Mater. Sci. Eng. A **473**, 189 (2008)

Publisher's Note Springer Nature remains neutral with regard to jurisdictional claims in published maps and institutional affiliations.